Supplementary Information

Electronic-structure descriptor-guided design of high-entropy perovskites for efficient CO_2 electrolysis

Nan Zhang,†[a] Caijin Xiao,†[c] Baixi Xia,[a] Beibei He,*[a] Xunxun Deng,[a] Ling Zhao,*[b] and Yida Deng*[a]

a State Key Laboratory of Tropic Ocean Engineering Materials and Materials Evaluation, School of Materials Science and Engineering, Hainan University, Haikou 570228, China

b School of Marine Science and Engineering, Hainan University, Haikou 570228, PR China

c Department of Nuclear Physics, China Institute of Atomic Energy, Beijing 102413, PR China

† *Equally contributed author.*

Corresponding author:Beibei He, E-mail: hebb@hainanu.edu.cn

Experimental section

Material Synthesis

The cathode materials $La_{1/2}Sr_{1/2}FeO_{3-\delta}$ (LSF), $La_{1/6}Sr_{1/6}Li_{1/6}Ba_{1/6}Ca_{1/6}Sm_{1/6}FeO_{3-\delta}$ (HE-LSF-Sm) and $La_{1/6}Sr_{1/6}Li_{1/6}Ba_{1/6}Ca_{1/6}Nd_{1/6}FeO_{3-\delta}$ (HE-LSF-Nd) were synthesized using a traditional sol-gel method. Stoichiometric amounts of nitrate precursors $La(NO_3)_3 \cdot 6H_2O$ (99%, Aladdin) $Sr(NO_3)_2$ (99.5%, Aladdin), $Fe(NO_3)_3 \cdot 9H_2O$ (AR, Sinopharm),$Ba(NO_3)_2$ (99.5%, Sinopharm), $Ca(NO_3)_2 \cdot 4H_2O$ (AR, Sinopharm), $LiNO_3$ （99.99%, Aladdin）, $Sm(NO_3)_3 \cdot 6H_2O$ (99.99%, Aladdin), $Nd(NO_3)_3$ (99.9%, Aladdin), citric acid (CA) (99.5%, Aladdin), and ethylenediaminetetraacetic acid (EDTA, 98%, Macklin) with the ratio of 1:1.5:1 was dissolved into deionized water. Then added $NH_3 \cdot H_2O$ (AR, Sinopharm) to adjust the pH to 7. The solution was heated under 200 ℃ until self-ignition occurred, forming a black precursor, which was calcined at 1050 °C for 5 h. The Functional layer $Gd_{0.1}Ce_{0.9}O_{2-\delta}$ (GDC) and anode $PrBa_{0.5}Sr_{0.5}Co_{1.5}Fe_{0.5}O_{5+\delta}$ (PBSCF) powders were also prepared using the same method.

Material characterization

Powder X-ray diffraction (XRD) was performed on a Bruker D8-Advance diffractometer to determine crystal structures. Morphology was examined using scanning electron microscopy (SEM, Hitachi SU-8010). For detailed structural characterization, high-resolution transmission electron microscopy (TEM) along with energy-dispersive spectrum (EDS) analysis were conducted on an FEI Talos F200x. Surface elemental states were probed using X-ray photoelectron spectroscopy (XPS) with a MULT1LAB2000 VG instrument. Oxygen vacancies were evaluated via electron paramagnetic resonance (EPR)

spectroscopy with a JES-FA300 instrument. CO_2 adsorption behavior was investigated using quasi in situ Fourier transform infrared (FTIR) spectroscopy. In the *in situ* FTIR test, sample powder was initially pretreated at 600 °C under a N_2 atmosphere to eliminate adsorbed species. Subsequently, CO_2 adsorption was conducted under a flow of CO_2 (50 mL min^{-1}) for 1 hour. Gaseous CO_2 was then swept away using N_2, the spectra were then collected under a N_2 flow at 600 °C. Neutron depth profiling (NDP) measurements were performed on the CARR Neutron Depth Profiling system (CARRNDP) situated at the China Advanced Research Reactor (CARR). Its operational mechanism relies on the nuclear reaction of ^{6}Li, of which the natural lithium isotope composition has a relative atomic abundance of 7.5 at%—with neutrons, which is described by the following reaction equation:

$$^6Li + n \rightarrow {}^4He\ (2055\ keV) + {}^3H\ (2727\ keV)$$

For depth calibration, the Stopping and Range of Ions in Matter (SRIM) code was adopted to establish a quantitative correlation between the detected particle energy (E) and the depth of charged particle generation inside the sample. This correlation enables the accurate calculation of the residual energy of charged particles emitted from different depth positions within the sample matrix.

Cell Fabrication and Electrochemical testing

Electrical conductivity of the dense strip (5.0 mm × 1.5 mm × 20.0 mm) in different atmospheres was collected via a DC four-point probe method on a digital multimeter Keithley2010. Electrical conductivity relaxation (ECR) was conducted by changing the atmosphere from 2:1 CO: CO_2 to 1:1 CO: CO_2. Electrochemical impedance spectroscopy (EIS) was conducted in a 1:1 CO: CO_2 atmosphere with the frequency ranges from 1 MHz

to 0.01 Hz. The $La_{0.8}Sr_{0.2}Ga_{0.8}Mg_{0.2}O_{3-\delta}$ (LSGM, Full Cell Materials) disk was prepared via a dry pressing process and then calcined at 1400 °C for 5 hours. Single cells with a (HE-LSF-Sm or HE-LSF-Nd or LSF) |GDC|| LSGM || PBSCF (anode) configuration were fabricated by screen-printing cathode and anode slurries (prepared in terpineol) onto the LSGM substrate and calcining at 1050 °C for 4 hours. The performance of SOECs was evaluated using an electrochemical workstation (Reference 3000, Gamry). The cathode was supplied with pure CO_2 at a flow rate of 40 mL min^{-1}, while the anode was exposed to air.

DFT Calculations

All simulations were performed using density functional theory (DFT) as implemented in the Vienna Ab initio Simulation Package (VASP)[1]. To calculate all-electron properties more efficiently, the Perdew-Burke-Ernzerhof (PBE) exchange-correlation together with generalized gradient approximation (GGA)[2]. A plane-wave kinetic-energy cutoff of 520 eV was applied for all calculations. The Brillouin zone of the 2×3×2 supercells was sampled using a 2×2×2 Monkhorst-Pack k-point mesh. For GGA + U calculations, the U values were adopted as depicted in **Supplementary Table 7**. The slab models were cleaved along the (001) surface, and a vacuum layer of 25 Å was introduced. All models were randomly generated with 10 distinct A-site atomic arrangement configurations, and the lowest energy configuration was selected as the basis for all subsequent calculations. Identical site standards were adopted for the selection of adsorption active sites, oxygen vacancy configurations, and reaction pathways. Ab Initio Molecular Dynamics (AIMD) simulations were carried out in the canonical NVT ensemble,

using a Nosé-Hoover thermostats. A time step of 2.0 fs was used, and simulations were conducted at 1073 K to probe the thermal stability and dynamical behavior.

Data collection and model training

A DFT-derived dataset comprising 230 perovskite oxides with diverse A-site chemistries was constructed. The original features included formula entropy (ΔS_{config}), A-site atomic number (Z_a), A-site ionization energy (E_a), A-site electronegativity (χ_a), A-site radius (R_a), A-site Lewis acid strengths (LAS_a), A-site group number (g_a), A-site period number (p_a), A-site mass (m_a), A-site valence electron number (N_{va}), A-site polarizability (r_{pola}), and tolerance factor (t). The inherent physicochemical characteristic values of the elements are shown in **Table S8 (**Supporting Information). To further explore the inherent correlations among features, a set of derived descriptors was generated based on feature-correlation analysis. These included electronegativity mismatch between A-site and B-site ($\Delta\chi_{a\text{-}b}$), combined radius-electronegativity ($R\times\chi$), product of entropy-ionization energy ($\Delta S_{config}\times E_a$), product of mass-ionization energy ($m_a\times E_a$), product of entropy-electronegativity ($\Delta S_{config}\times\chi$), polarization density (p_{pol}), product of entropy-polarizability ($\Delta S_{config}\times r_{pola}$), Lewis acid strength per radius (LAS_a/R_a), polarizability density (α), ionic potential (φ), mass per unit volume (m/R^3), ionization energy per radius (E_a/R), product of mass and radius ($m_a\times R_a$), polarizability per unit mass (α/m_a), squared radius (R_a^2), and logarithm of mass ($\log(m_a)$).

The whole learning-assisted dataset was randomly split into a training set (70%, 161 samples) and a test set (30%, 69 samples). Five regression models, AdaBoost, random forest (RF), linear regression (LR), K nearest neighbors (KNN) and feedforward neural network (FNN) were implemented to predict the ε_p. Hyperparameters for each model were

optimized using a grid-search strategy with cross-validation. After training and hyperparameters optimization, adopted the determination (R^2) and root mean square error (RMSE) to evaluation the ML models. To interpret model predictions, SHapley Additive exPlanations (SHAP) were employed to quantify the contribution of each descriptor to the predicted target values.

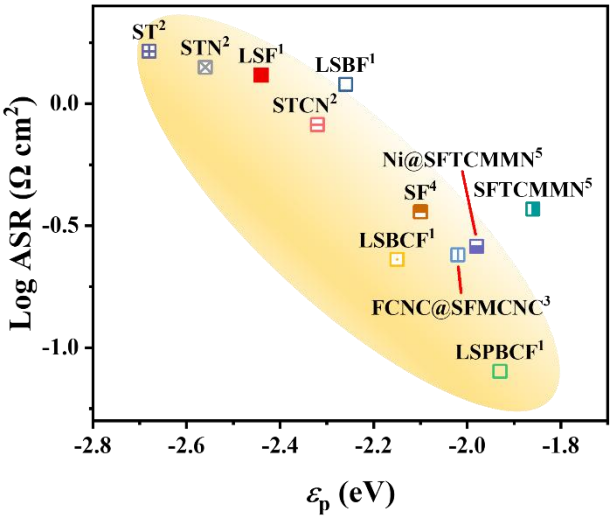

Figure S1. Experimental area specific resistances (ASR) vs the calculated ε_p at 800 °C and 1.2 V [3-7].

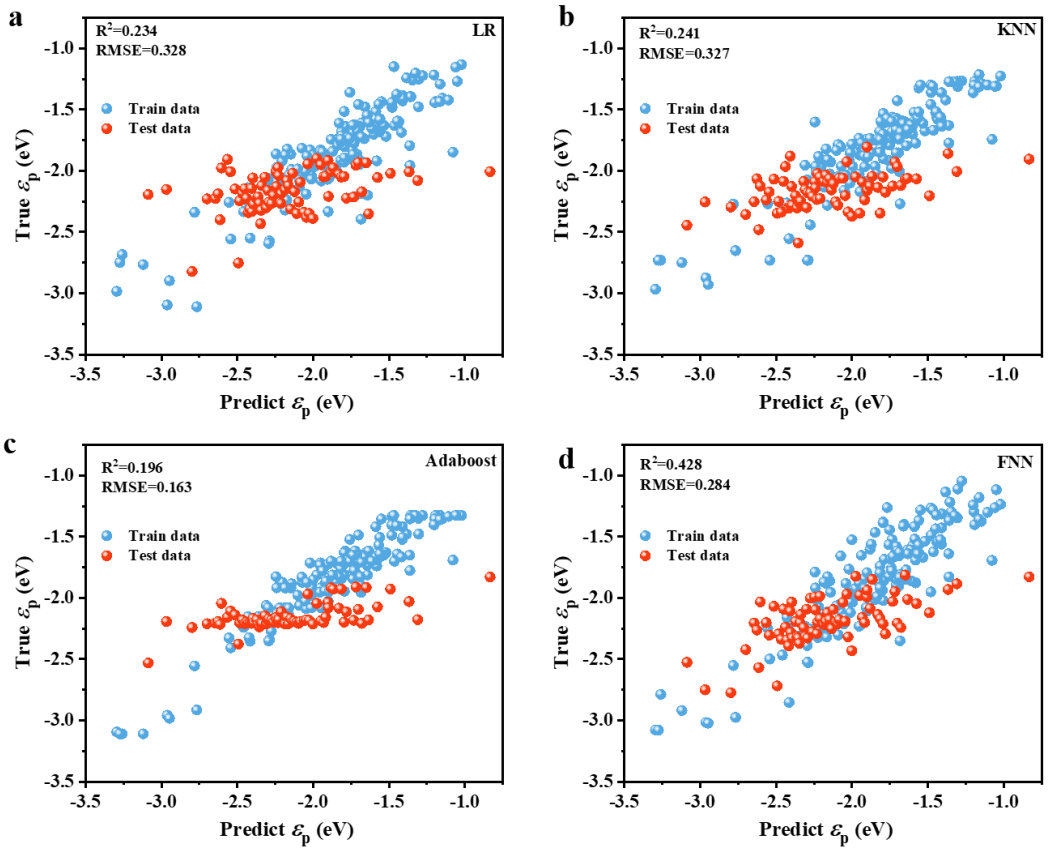

Figure S2. Scatter plot of true ε_p vs. predicted ε_p of a) LR, b) KNN, c) Adaboost, and d) FNN.

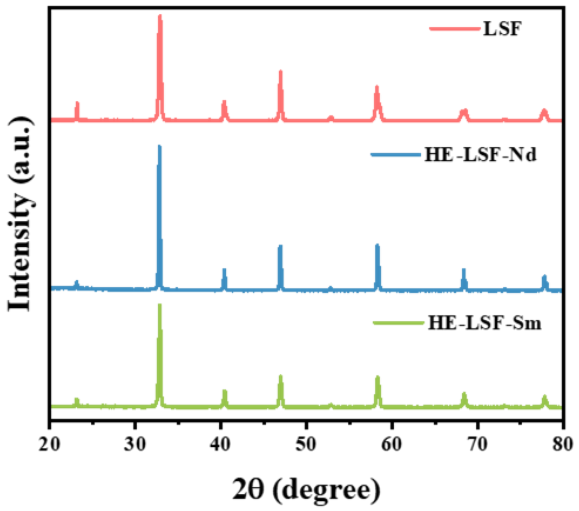

Figure S3. XRD patterns of LSF, HE-LSF-Sm, HE-LSF-Nd electrocatalysts.

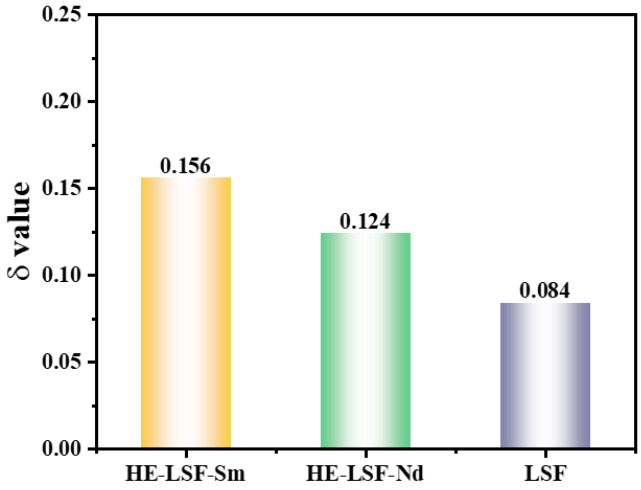

Figure S4. The oxygen non-stoichiometries (δ) of HE-LSF-Sm, HE-LSF-Nd and LSF at room temperature.

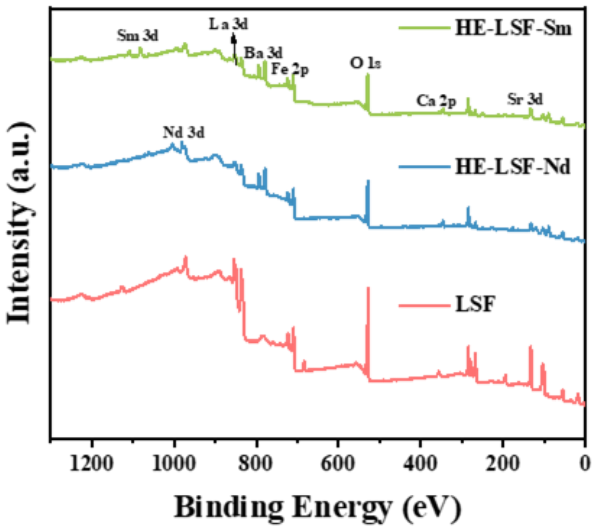

Figure S5. XPS full survey spectra of HE-LSF-Sm, HE-LSF-Nd, and LSF electrocatalysts.

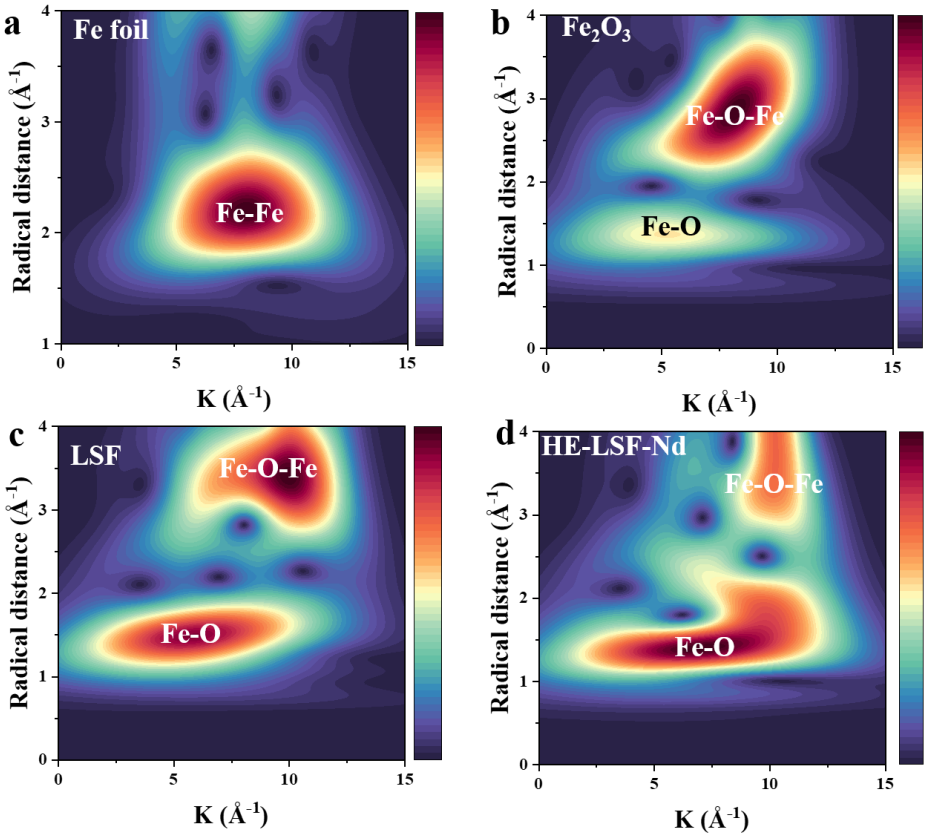

Figure S6. Wavelet transform analysis of Fourier transformed EXAFS spectra for a) HE-LSF-Nd, b) LSF, c) Fe_2O_3, and d) Fe foil.

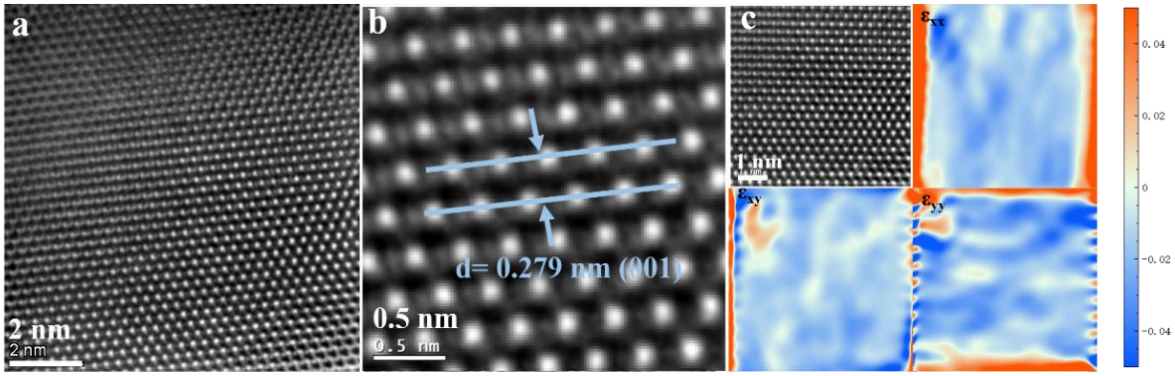

Figure S7. HAADF-STEM images of a-b) LSF electrocatalyst. The corresponding GPA images of c) LSF electrocatalyst.

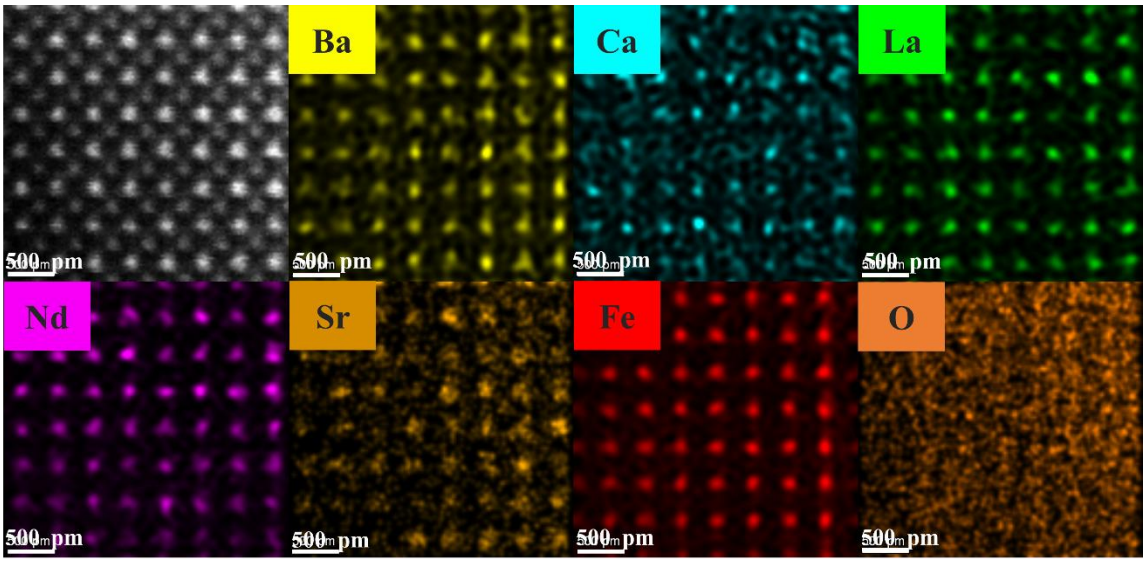

Figure S8. Atomic-scale EDS elemental maps of HE-LSF-Nd electrocatalyst.

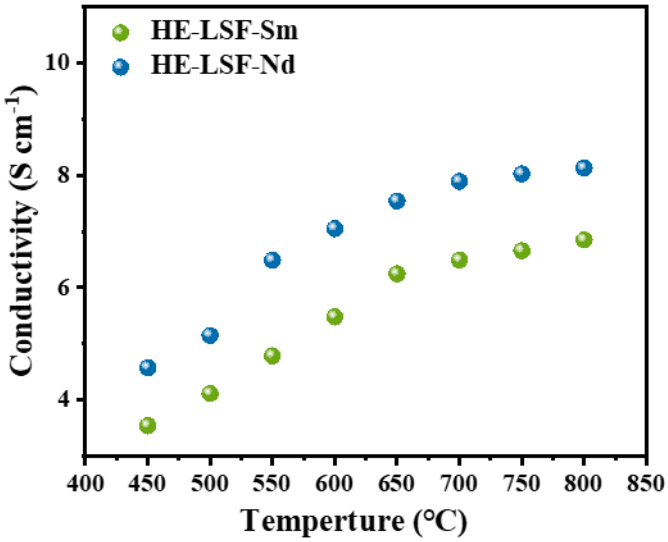

Figure S9. Electrical conductivities of HE-LSF-Sm and HE-LSF-Nd under CO/CO_2=1:1 atmosphere.

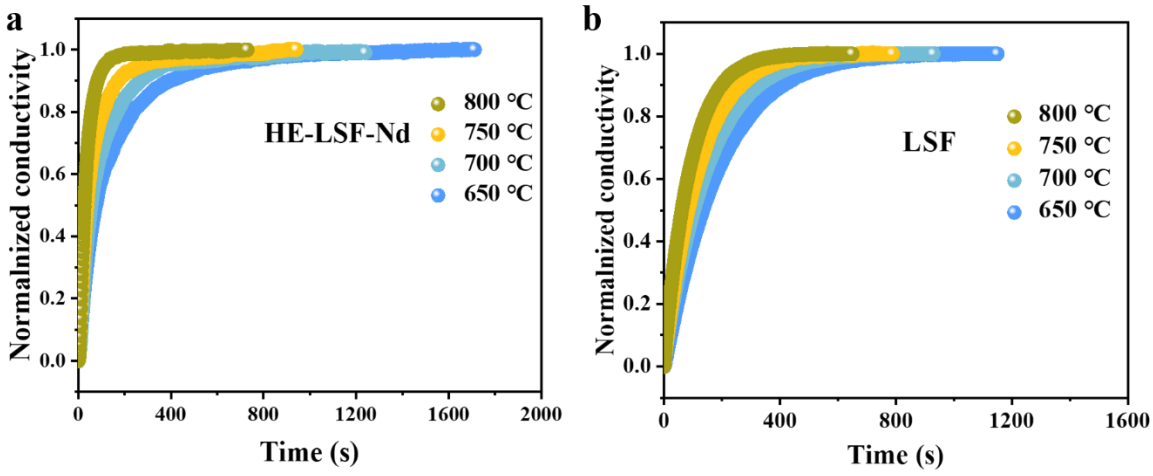

Figure S10. Normalized conductivity curves of HE-LSF-Nd and LSF electrocatalysts at different temperature.

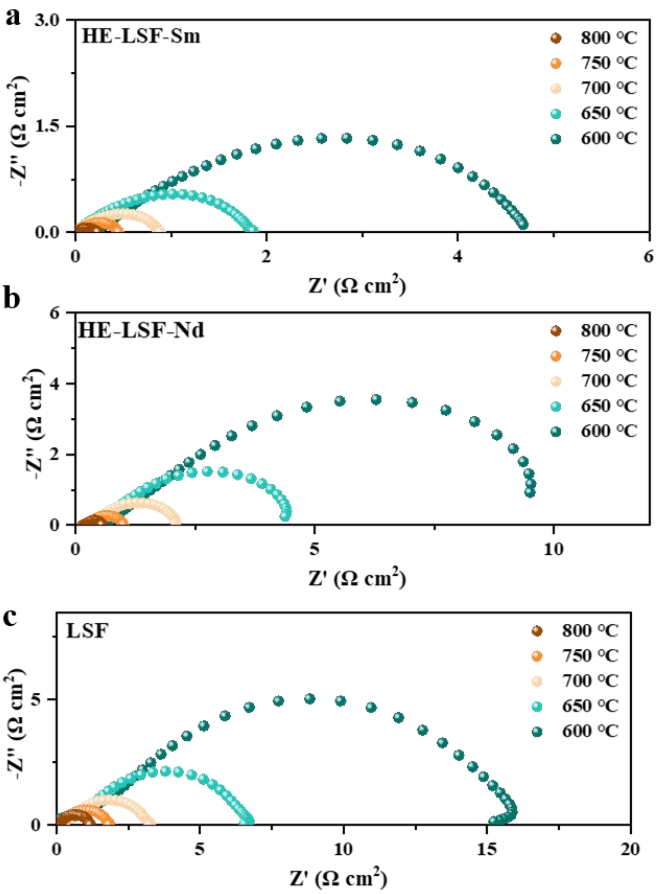

Figure S11. Nyquist plots of a) HE-LSF-Sm and b) HE-LSF-Nd electrodes measured at 600-800 ℃.

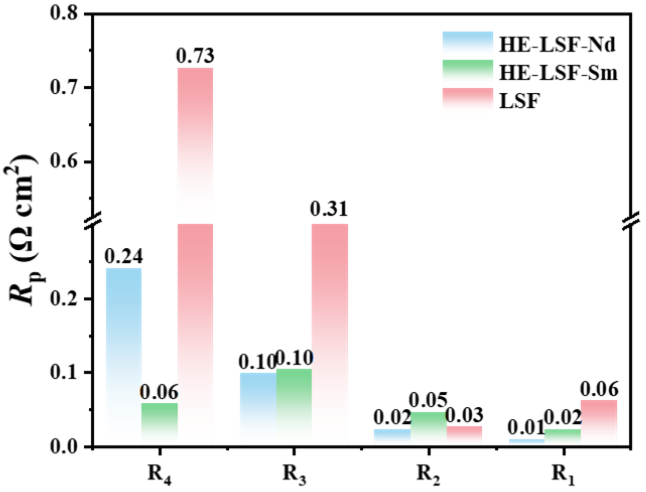

Figure S12. The corresponding fitted R_p value of LSF, HE-LSF-Sm and HE-LSF-Nd electrodes by DRT analysis.

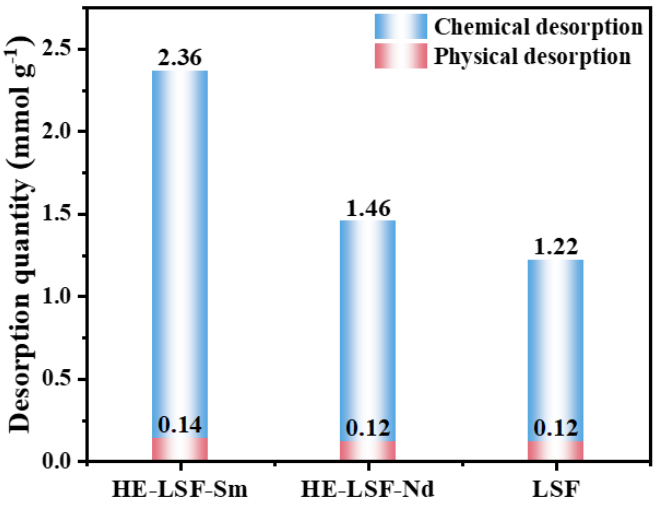

Figure S13. Chemical and physical desorption of CO_2-TPD for LSF, HE-LSF-Sm and HE-LSF-Nd electrocatalysts.

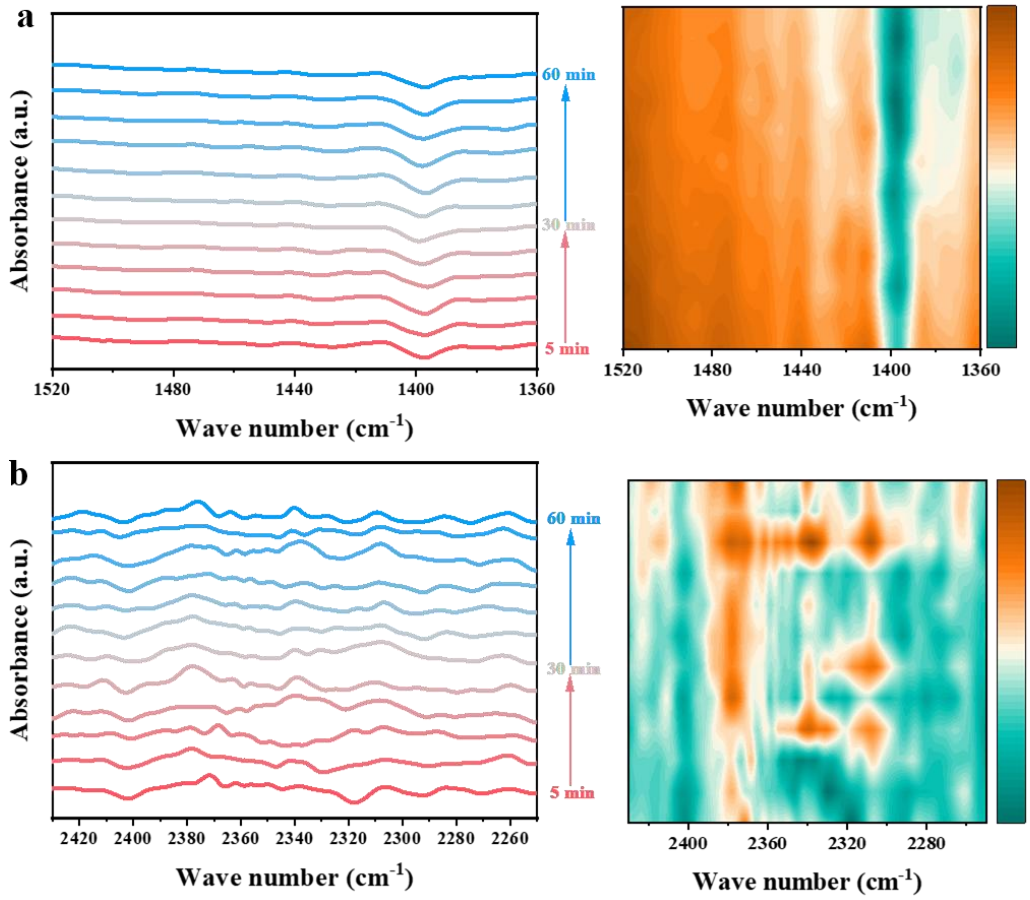

Figure S14. *In situ* IR spectra of LSF electrocatalyst in at various time at 650 °C under CO_2 atmosphere from a) 1520 to 1360 cm^{-1} and b) from 2430 to 2250 cm^{-1}.

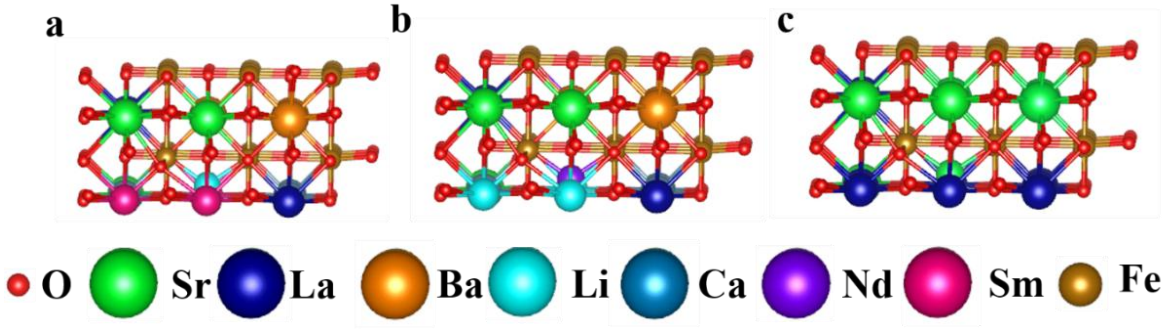

Figure S15. Theoretical modes of a) HE-LSF-Sm, b) HE-LSF-Nd and c) LSF.

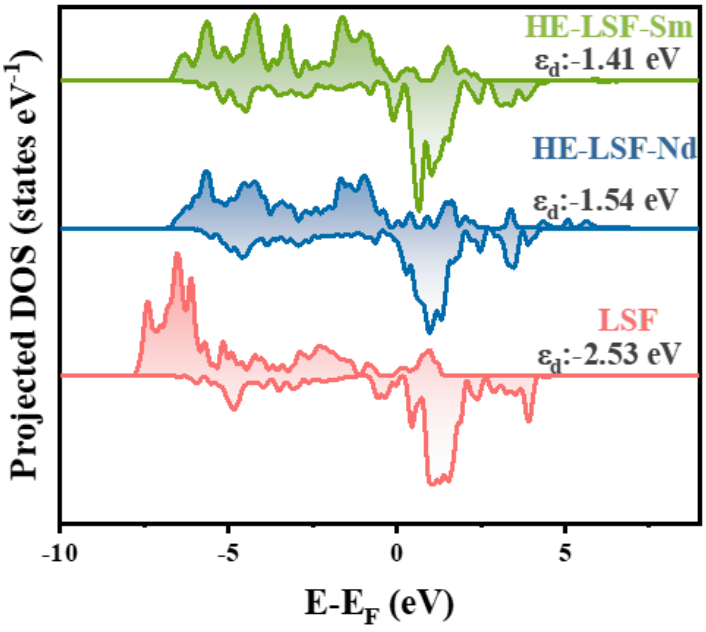

Figure S16. Density of states of Fe 3*d* orbit of HE-LSF-Sm, HE-LSF-Nd and LSF.

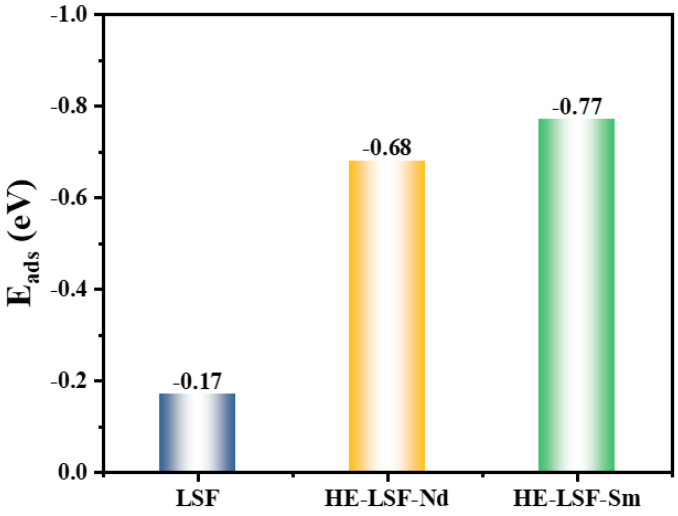

Figure S17. The CO_2 absorption energy (E_{ads}) of LSF, HE-LSF-Nd and HE-LSF-Sm.

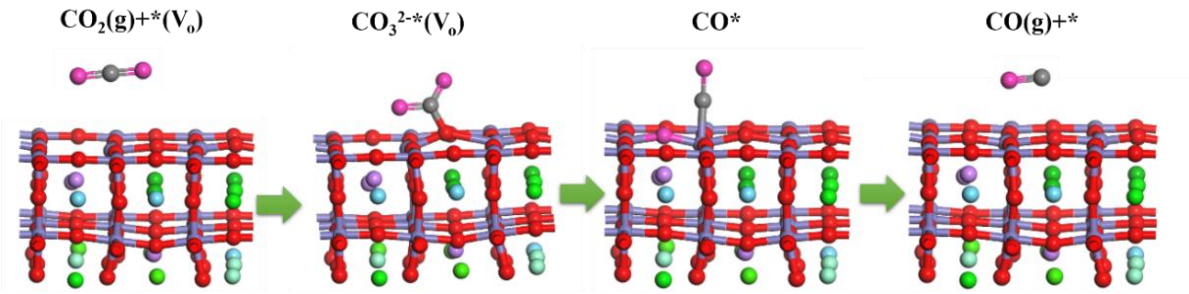

Figure S18. CO_2RR pathway of HE-LSF-Sm and HE-LSF-Nd. (The gray spheres represent the C in CO_2, the pink spheres denote the O derived from CO_2, and the red spheres stand for the O in the perovskite).

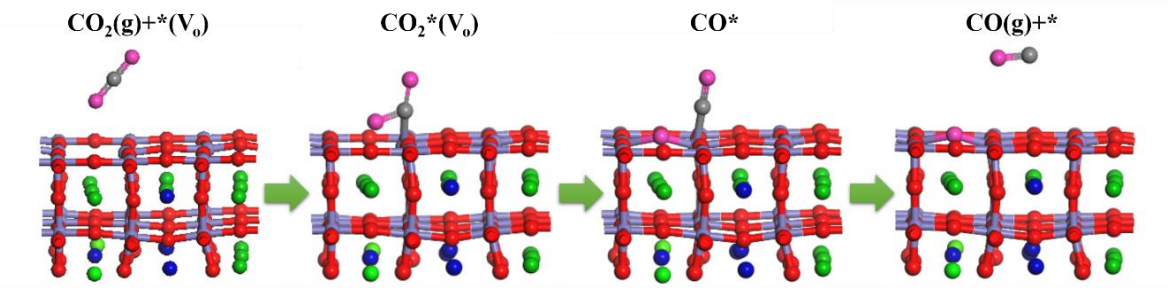

Figure S19. CO_2RR pathway of LSF (The gray spheres represent the C in CO_2, the pink spheres denote the O derived from CO_2, and the red spheres stand for the O in the perovskite).

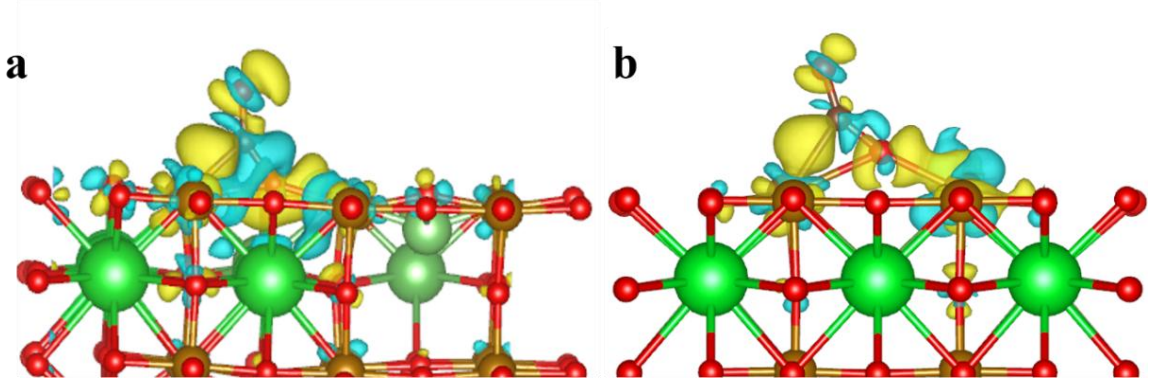

Figure S20. Differential charge density maps of a) HE-LSF-Nd and b) LSF electrocatalysts.

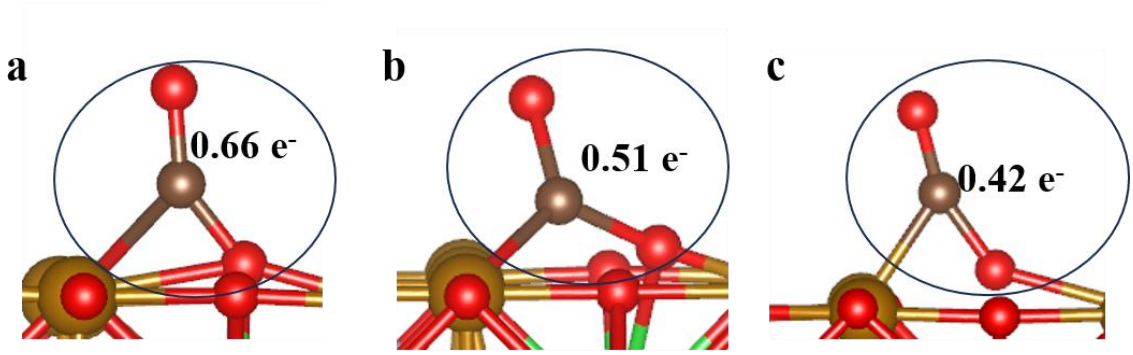

Figure S21. Bader charge analysis of a) HE-LSF-Sm, b) HE-LSF-Nd and c) LSF.

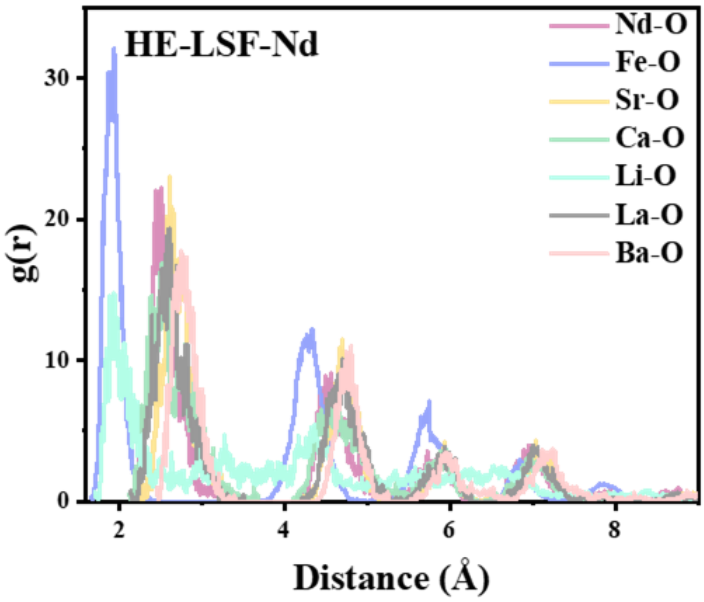

Figure S22. Radial distribution functions (g(r)) of cation-oxygen pairs for HE-LSF-Nd electrocatalyst.

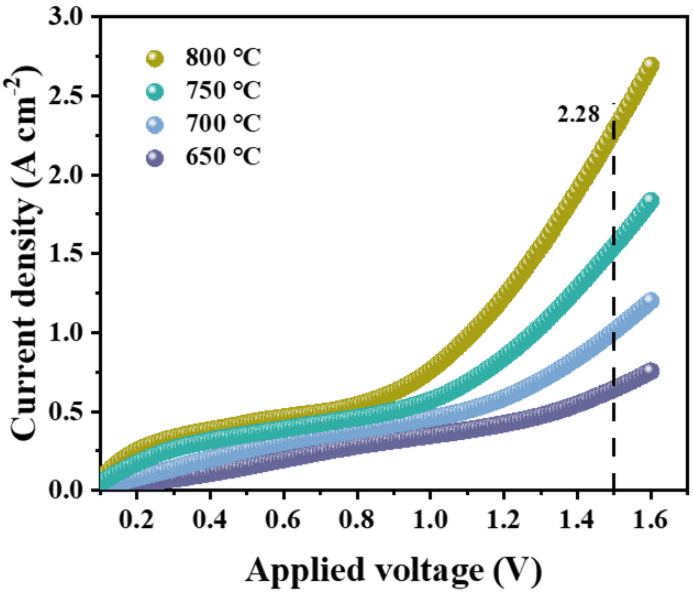

Figure S23. *I-V* curves of single cells based on HE-LSF-Nd cathode measured at 650-800 ℃.

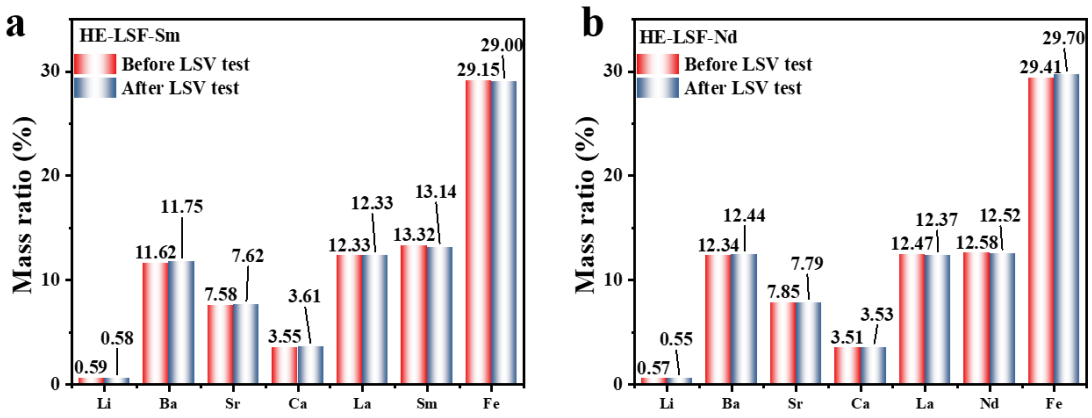

Figure S24. ICP-OES analysis of HE-LSF-Sm and HE-LSF-Nd cathodes before and after LSV test.

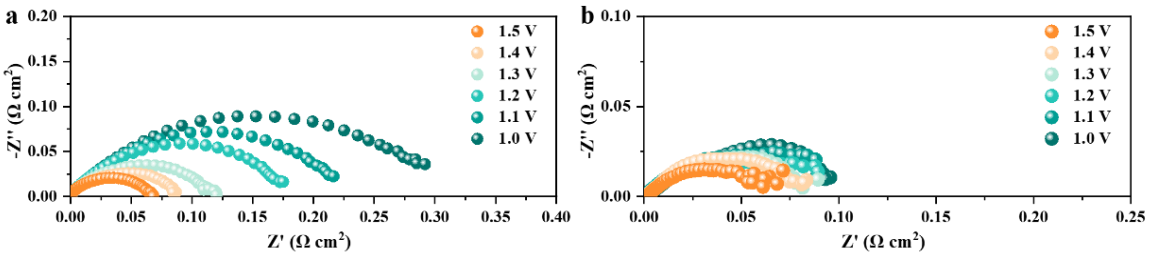

Figure S25. EIS spectra of (a) HE-LSF-Sm, and (b) HE-LSF-Nd cathodes measured at 800 ℃ and recorded at an applied voltage of and 1.0-1.5 V.

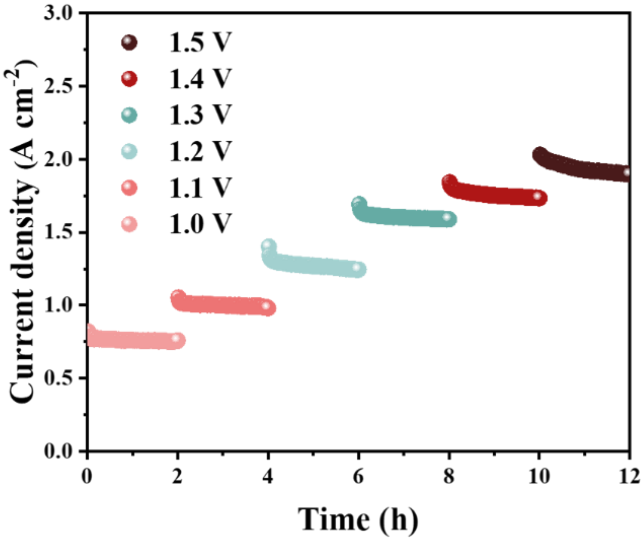

Figure S26. Short-term stability test of HE-LSF-Nd based SOEC at 800 °C and different voltages.

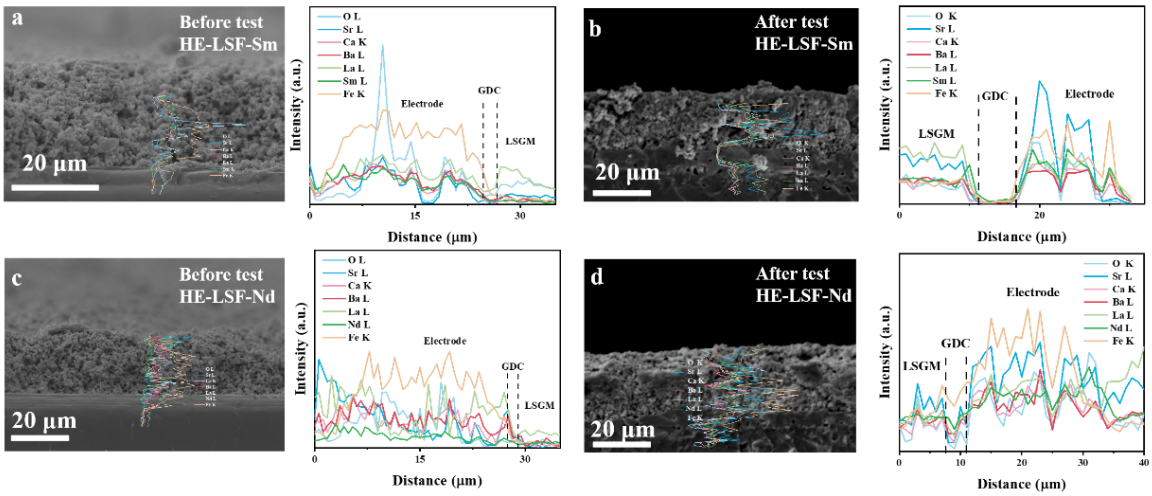

Figure S27. SEM images after long-term operation and corresponding EDS elemental line scanning of a) HE-LSF-Sm based SOEC, b) HE-LSF-Nd based SOEC (left: before test, right: after test).

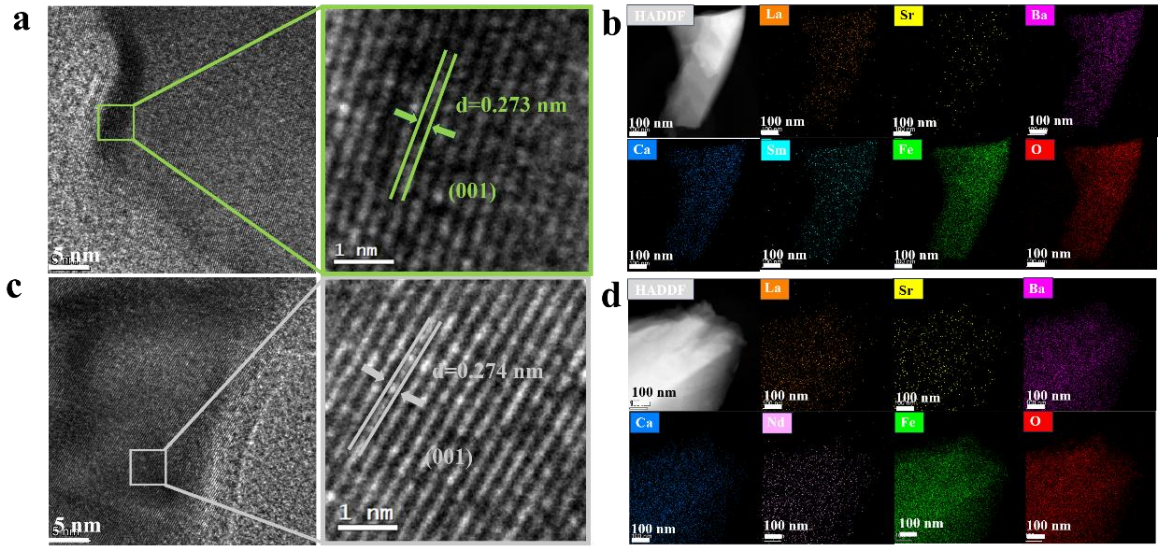

Figure S28. HR-TEM images of a) HE-LSF-Sm, b) HE-LSF-Nd electrocatalysts and corresponding EDS element mapping of b) HE-LSF-Sm, d) HE-LSF-Nd electrocatalysts after long-term test.

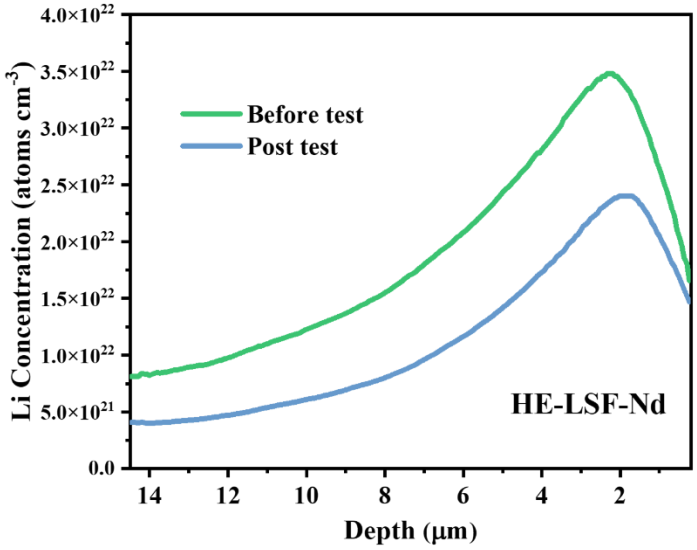

Figure S29. Time-resolved lithium concentration profiles of HE-LSF-Nd cathode before and after the stability test.

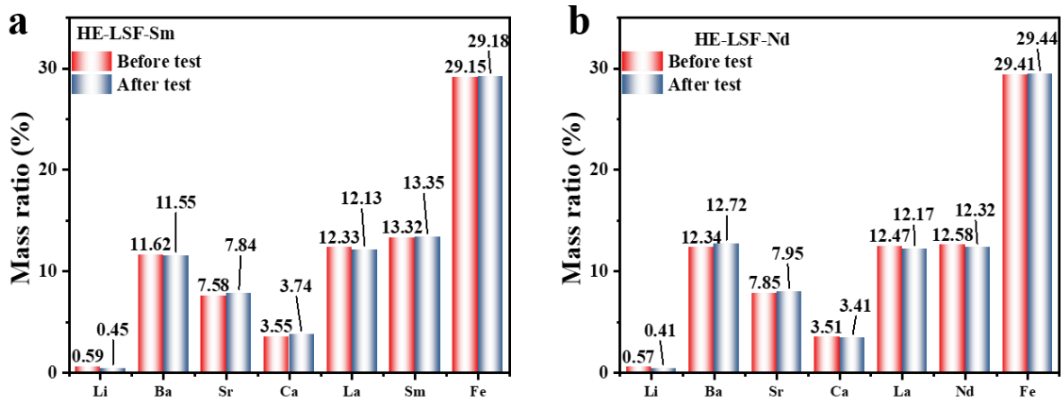

Figure S30. ICP-OES analysis of HE-LSF-Sm and HE-LSF-Nd cathodes before and after long-term operation.

Tabel S1 R^2 and RMSE of the as-investigated LR, KNN, FNN, Adaboost and RF models.

Model	R^2	RMSE
LR	0.234	0.328
KNN	0.241	0.327
FNN	0.428	0.284
Adaboost	0.196	0.336
RF	0.872	0.163

Tabel S2. Lattice parameters of HE-LSF-Sm, HE-LSF-Nd and LSF obtained from XRD Rietveld refinement.

Electrocatalysts	Space group	a=b=c (Å)	α=β =γ (°)	R_p (%)	R_{wp}(%)	χ^2
HE-LSF-Sm	*Pm-3m*	3.8426	90	7.55	8.59	6.75
HE-LSF-Nd	*Pm-3m*	3.8606	90	6.15	8.32	6.55
LSF	*Pm-3m*	3.9019	90	4.95	6.41	2.05

Tabel S3. Average bonding energy of metal-oxygen for HE-LSF-Sm, HE-LSF-Nd and LSF electrocatalysts samples.

Sample	<A–O> (kJ mol^{-1})						<B–O>	<ABE>
HE-LSF-Sm	<Li–O>	<La–O>	<Sr–O>	<Ca–O>	<Ba–O>	<Sm-O>	<Fe–O>	-229.36
	-8.03861	-23.6526	-13.9636	-14.7406	-14.7587	-20.7412	-133.471	
HE-LSF-Nd	<Li–O>	<La–O>	<Sr–O>	<Ca–O>	<Ba–O>	<Nd-O>	<Fe–O>	-230.93
	-8.03861	-23.6526	-13.9636	-14.7406	-14.7587	-22.3092	-133.471	
LSF		<La–O>			<Sr–O>		<Fe–O>	-246.32
		-70.9578			-41.8908		-133.471	

Tabel S4. The concentration summary of various Fe species and the average valence.

Sample	Fe^{2+}	Fe^{3+}	Fe^{4+}	Average valence
HE-LSF-Sm	30.98	41.12	27.90	2.97
HE-LSF-Nd	28.32	43.19	28.49	3.00
LSF	24.22	46.69	29.09	3.05

Tabel S5. The concentration summary of various O species.

Electrocatalysts	O_{latt}	O_{ads}		H_2O	$O_{ads}/(O_{ads}+O^{2-}+H_2O)$
		O^-/O_2^{2-}	OH^-/CO_3^{2-}		
LSF	42.56	17.62	25.71	14.11	43.33
HE-LSF-Nd	33.42	29.97	27.49	9.12	57.46
HE-LSF-Sm	28.4	31.29	29.87	10.44	61.16

Tabel S6. Electrochemical performance of the current cathodes this work at 1.5 V compared with representative state-of-the-art cathodes of SOEC.

Cathode	Temperature (℃)	Current density (A cm^{-2})	Time (h)	Refs.
HE-LSF-Sm	800	2.55	>900	This work
	750	1.73		
	700	1.2		
	650	0.87		
HE-LSF-Nd	800	2.28	>900	This work
	750	1.56		
	700	1		
	650	0.63		
F-SFM	800	1.56	180	8
	750	0.82		
	700	0.67		
	650	0.52		
SLFM	800	1.68	35	9
	750	1.1		
	700	0.59		
SFCuM-R	800	2.3	100	10
	750	1.45		
	700	0.78		
SF1.5M-R	800	1.41	130	11
	750	0.9		
	700	0.53		
	650	0.25		
SFMC-GDC	800	1.16	50	12
	750	0.79		
	700	0.46		
SF1.5MC-GDC	800	2.24	80	13
	750	1.51		
	700	0.91		
	650	0.52		
STCF	800	0.5	20	14
	750	0.32		
	700	0.26		
LSCFP	800	2.24	120	15
	750	1.39		
	700	0.75		
Cl-SFM	800	2.09	500	16
	750	0.92		

	700	0.51		
RFA@FeO_x/PBFRH	800	1.5	400	[17]
	750	0.92		
	700	0.5		
SFMV	800	1.59	300	[18]
	750	0.95		
	700	0.54		
	650	0.27		

Chemical formula of the electrode materials mentioned above:

F-SFM: $Sr_2Fe_{1.5}Mo_{0.5}O_{6-\delta}F_{0.1}$

SLFM: $(La_{0.75}Sr_{0.25})_{0.97}Cr_{0.5}Mn_{0.5}O_3$

SFCuM-R: $Sr_2Fe_{1.25}Cu_{0.25}Mo_{0.5}O_{6-\delta}$

SF1.5M-R: $Sr_2Fe_{1.5}Mo_{0.5}O_{6-\delta}$

SFMC-GDC: $Sr_2Fe_{1.35}Mo_{0.45}Co_{0.2}O_{6-\delta}$

SF1.5MC-GDC: $Sr_2Fe_{1.5}Mo_{0.3}Cu_{0.2}O_{6-\delta}$

STCF: $Sr_2Ti_{0.8}Co_{0.2}FeO_{6-\delta}$

LSCFP: $La_{0.6}Sr_{0.4}Co_{0.15}Fe_{0.8}Pd_{0.05}O_{3-\delta}$

Cl-SFM: $Sr_2Fe_{1.5}Mo_{0.5}O_{5.95-\delta}Cl_{0.05}$

RFA@FeOx/PBFRH: RuFe alloy@FeO_x/$Pr_{0.9}Ba_{0.9}Fe_{1.7}Hf_{0.2}Ru_{0.1}O_{5+\delta}$

SFMV: $Sr_2Fe_{1.5}Mo_{0.4}V_{0.1}O_{6-\delta}$

Tabel S7. Hubbard (U–J) values used in DFT+U calculations.

Element	U–J (eV)
Li	0
Na	0
K	0
Mg	0
Ca	0
Sr	0
Ba	0
Bi	0
La	0
Nd	6.0
Pr	5.0
Sm	6.0
Eu	6.5
Gd	6.0
Y	3.0
O	0
Fe	4.0

Tabel S8. Fundamental physicochemical properties of constituent ions.

Element	Z	R(Å)	χ	E (eV)	LAS	g	p	m	N_v	r_{pol}
Na	11	1.39	0.93	5.14	0.108	1	4	22.99	1	43.4
Mg	12	1.03	1.31	7.65	0.264	2	4	24.31	2	18.8
K	19	1.64	0.82	4.34	0.099	1	5	39.10	1	52.9
Li	3	0.76	0.98	5.39	0.025	1	2	6.94	1	24.3
Ca	20	1.34	1.00	6.11	0.222	2	5	40.08	2	24.3
Sr	38	1.44	0.95	5.69	0.194	2	6	87.62	2	30.5
Y	39	1.28	1.22	6.22	0.326	3	6	88.91	3	35.0
Ba	56	1.61	0.89	5.21	0.320	3	6	137.33	2	39.8
La	57	1.36	1.30	5.58	0.326	3	6	138.91	3	39.0
Pr	59	1.32	1.40	5.47	0.380	3	6	140.91	3	36.9
Nd	60	1.27	1.14	5.53	0.371	3	6	144.24	3	35.0
Sm	62	1.24	1.17	5.64	0.371	3	6	150.36	3	34.5
Eu	63	1.20	1.20	5.67	0.375	3	6	151.96	3	33.7
Gd	64	1.18	1.39	6.15	0.396	3	6	157.25	3	33.0
Bi	83	1.03	2.02	7.29	0.450	3	6	208.98	5	10.8
Fe	26	0.645	1.83	7.90	0.460	3	4	55.85	5	21.0
O	8	1.40	3.44	13.62	0	2	2	16.00	6	2.0

References

1. G. Kresse and J. Furthmüller, *Phy. rev. B*, 1996, **54**, 11169.
2. J. P. Perdew, J. A. Chevary, S. H. Vosko, K. A. Jackson, M. R. Pederson, D. J. Singh and C. Fiolhais, *Phy. rev. B*, 1992, **46**, 6671.
3. N. Zhang, W. Zhang, M. Wu, R. Wang, Y. Gong, H. Wang, J. Jin, L. Zhao and B. He, *J. Colloid Interface Sci.*, 2025, **682**, 70-79.
4. X. He, X. Huang, H. Sun and L. Gan, *Journal of Power Sources*, 2025, **654**, 237855.
5. S. Liu, L. Liu, M. Yang, Y. Li, Q. Pan, Y. Sun, X.-Z. Fu, S. Liu and J.-L. Luo, *Chem. Eng. J.*, 2025, **519**, 165404.
6. Y. Fan, Y. Yi, Y.-H. Liu, X. Xi, J. Liu, I. Starostina, D. Medvedev, J. Zhang, X.-Z. Fu and J.-L. Luo, *ACS Catal.*, 2025, **16**, 380-391.
7. C. Wang, Y. Zhu, L. Zhao, R. Wang, J. Jin, Y. Gong, H. Wang and B. He, *Sep. Purif. Technol.*, 2025, **354**, 128950.
8. Y. Li, Y. Li, Y. Wan, Y. Xie, J. Zhu, H. Pan, X. Zheng and C. Xia, *Adv. Energy Mater.*, 2018, **9**, 1803156.
9. S. Lee, M. Kim, K. T. Lee, J. T. S. Irvine and T. H. Shin, *Adv. Energy Mater.*, 2021, **11**, 2100339.
10. X. Xi, Y. Fan, J. Zhang, J. Luo and X. Z. Fu, *J. Mater. Chem. A*, 2022, **10**, 2509-2518.
11. X. Xi, J. Liu, W. Luo, Y. Fan, J. Zhang, J. L. Luo and X. Z. Fu, *Adv. Energy Mater.*, 2021, **11**, 2102845.
12. H. Lv, L. Lin, X. Zhang, Y. Song, H. Matsumoto, C. Zeng, N. Ta, W. Liu, D. Gao, G. Wang and X. Bao, *Adv. Mater.*, 2020, **32**, e1906193.
13. F. He, M. Hou, F. Zhu, D. Liu, H. Zhang, F. Yu, Y. Zhou, Y. Ding, M. Liu and Y. Chen, *Adv. Energy Mater.*, 2022, **12**, 2202175.
14. B. Niu, C. Lu, W. Yi, S. Luo, X. Li, X. Zhong, X. Zhao and B. Xu, *Appl.Catal. B Environ.*, 2020, **270**, 118842.
15. A. Akhmadjonov, K. T. Bae and K. T. Lee, *Nanomicro Lett.*, 2024, **16**, 93.
16. S. Zhang, X. Hu, T. Liu, H. Liu, Y. Guo, G. Zou, W. Zhang, X. Zhang, P. Zhang, R. Yu, Y. Song, C. Xia, G. Wang and X. Bao, *Adv. Mater.*, 2025, 202518116.
17. Y. Zhu, X. Li, L. Zhao, N. Zhang, B. He and Y. Deng, *Appl. Catal. B Environ.*, 2026, **381**, 125812.
18. Y. Zhu, N. Zhang, W. Zhang, L. Zhao, Y. Gong, R. Wang, H. Wang, J. Jin and B. He, *ACS Appl. Mater. Interf.*, 2024, **16**, 36343-36353.